Journal of
Materials Chemistry A

ROYAL SOCIETY
OF CHEMISTRY

PAPER

View Article Online
View Journal | View Issue

Cite this: *J. Mater. Chem. A*, 2023, **11**, 25455

Dense cuprous oxide sheath decorated three-dimensional copper foam enabling stable lithium metal anodes†

Chengcai Liu,[a] Borong Wu, *[abc] Yuanxing Zhang, [a] Tao Liu,[b] Jingwen Cui,[b]
Lingjun Huang,[a] Guoqiang Tan,[ab] Ling Zhang, *[ab] Yuefeng Su[ab] and Feng Wu[ab]

Received 19th July 2023
Accepted 26th September 2023

DOI: 10.1039/d3ta04259f

rsc.li/materials-a

Uneven lithium deposition causing the growth of lithium dendrites is a major obstacle to the practical application of high-energy lithium metal batteries. In this study, a simple hydrothermal reaction is adopted to evenly coat copper foam (CF) with cuprous oxide particles. The resulting three-dimensional composite current collector can achieve dendrite-free lithium plating. Control experiments show that FeF_3 is a better oxidant than $FeCl_3$ for creating a more uniform and dense cuprous oxide coating on the CF. It is also found that the reaction temperature plays a crucial role in determining the thickness of the coating layer. Furthermore, the electrochemical experimental results confirm that a dense and uniform coating layer with an appropriate thickness is essential in achieving high coulombic efficiency (CE) for CF current collectors. The CF with the optimal coating exhibits only a small nucleation overvoltage (15 mV) and high CE (98% retention after 120 cycles) at a current density of 1.0 mA cm^{-2} and a Li deposition of 1.0 mA h cm^{-2} in an ether electrolyte without lithium nitrate.

1. Introduction

Lithium metal anodes have received considerable attention due to their high specific capacity (3860 mA h g^{-1}, ten times higher than that of graphite) and low reduction potential (−3.04 V *vs.* the standard hydrogen electrode).[1] However, the non-uniform deposition of lithium ions can lead to the uncontrolled growth of implanted lithium and the unlimited volume change of lithium metal, which severely affects the performance of lithium metal batteries.[2] For instance, the growth of mossy lithium and dendrites increases the roughness of the metallic lithium surface, which enhances the reaction with the electrolyte. Moreover, lithium dendrites can lead to the rupture of the solid-electrolyte interphase (SEI) formed on the surface of metallic lithium, further promoting the occurrence of side reactions. This not only results in a significant loss of active lithium, but also leads to increased heat generation in the battery, ultimately causing thermal runaway.[3–6] In addition, the growth of dendrites tends to puncture the separator, resulting in a short circuit and further contributing to thermal runaway.[7] Additionally, the generation of lithium dendrites can cause the formation of dead lithium, increasing the battery impedance and reducing the utilization rate of metal lithium.[8] Due to the intrinsic feature of Li metal, which determines its unlimited volume change in electrochemical reactions, the SEI film can rupture, leading to side reactions between the electrolyte and exposed fresh lithium metal, and reducing the coulombic efficiency (CE) of the lithium metal battery.[9,10] Therefore, solving the aforementioned problems with lithium metal anodes is the key to realizing the commercialization of lithium metal batteries.[11] Scientists have proposed several strategies to address the issues around lithium metal anodes, for instance, modifying the surface of lithium metal (artificial SEI),[12–15] modifying the electrolyte (electrolyte additives),[16] modifying the separator,[17–19] modifying the current collector[20] or using a solid electrolyte with a high Young's modulus[21] and a three-dimensional (3D) current collector.[22,23] Among them, the use of a 3D current collector is a very effective method to address the issues associated with lithium metal anodes. Firstly, the 3D collector has a large specific surface area, which can reduce the local current density and slow down the growth rate of lithium dendrites.[24–30] Secondly, the 3D current collector has a large internal space, which can accommodate the deposited lithium metal, reduce the volume change of lithium metal, and stabilize the SEI. However, most of the 3D metal current collectors (Cu foam,[26] Ni foam,[23,31] metallic glass-fiber[32] and nitrogen-doped 3D carbon skeleton[33]) show poor affinity to Li, which can lead to a large nucleation over voltage in the initial lithium deposition stage, which is extremely unfavorable for the subsequent uniform deposition of lithium. Li ions prefer to nucleate on the

---

[a] *School of Material Science and Engineering, Beijing Institute of Technology, Beijing, 100081, China. E-mail: wubr@bit.edu.cn; zhangling2022@bit.edu.cn*

[b] *Chongqing Innovation Center, Beijing Institute of Technology, Chongqing, 401120, China*

[c] *Collaborative Innovation Center of Electric Vehicles in Beijing, Beijing 100081, China*

† Electronic supplementary information (ESI) available. See DOI: https://doi.org/10.1039/d3ta04259f

conductive junctions and accumulate on the top surface of 3D lithiophobic metal current collectors rather than inside the pores, which can damage the CE of lithium metal batteries.[26] Therefore, the 3D lithiophobic current collector itself does not exhibit uniform lithium deposition characteristics. Modifying lithiophilic materials can be a highly effective approach to achieve uniform Li deposition within the 3D current collector. For instance, lithiophilic silver nanoseeds anchored on a 3D carbon matrix can guide the uniform deposition of lithium metal, forming a dendrite-free Li metal anode.[34] Another example involves coating a 3D metal Ni current collector with graphene oxide, which enables the uniform coating and promises a dendrite-free Li metal anode. Graphene oxide provides numerous nucleation sites that promote the even deposition of lithium.[35] However, these methods are often complex and expensive, making them impractical for widespread use. Therefore, it is essential to develop a simple and effective method to modify the 3D collector for high-performance lithium metal anodes.

In this paper, we use oxidizing agents and copper foam (CF) under hydrothermal conditions to form a layer of Cu_2O on the surface of CF to enhance its lithium affinity. Fe^{3+} is often used as an etching metal copper because of its strong oxidation, and $FeCl_3$ is often selected as an oxidant because of its better solubility. However, when we used $FeCl_3$ to react with CF, we found that the structure of CF was severely damaged and lost its original flexibility and became very brittle. When assembling a half-cell, it was often easy to pierce the separator, making the battery unable to work. Here, a uniform Cu_2O coating layer on CF was prepared *via* a one-step hydrothermal method at a relatively low temperature using FeF_3 as an oxidant. When FeF_3 is used as an oxidant, the CF structure maintains its integrity and retains its original flexibility. The selection of Cu_2O to modify CF was based on its good affinity to lithium metal. Moreover, synthesis of a Cu_2O modified CF surface is facile and applicable for large-scale production. During the electrochemical reaction, the Cu_2O coating layer is transformed into lithium oxide (Li_2O) and copper coating layers. Li_2O is known to facilitate Li^+ transportation within the anode and ensure uniform Li^+ flux on the whole electrode surface due to its ability for uniform electric field distribution. Thus, the good lithiophilicity of the Cu_2O particle modified layer can significantly reduce the nucleation overvoltage of CF and achieve smooth lithium deposition, resulting in a stable CE of 98% for 120 cycles at a current density of 1 mA cm^{-2} and a capacity of 1 mA h cm^{-2}. Furthermore, the CE remained almost unchanged even with a double capacity of 2 mA h cm^{-2}, indicating excellent performance of the modified CF current collector.

2. Results and discussion

Fig. 1a displays the process of synthesizing the Cu_2O modified layer on CF. This involved using a saturated aqueous solution of FeF_3 to soak the CF piece and obtaining the Cu_2O coated layer by a one-step hydrothermal reaction at 80 °C, named CF-80. The morphologies of CF and the Cu_2O coating layer are shown in the insert SEM images. Fig. 1b illustrates the different lithium nucleation and plating processes on CF and CF-80 current collectors. Without modification, the lithium ions first nucleate on the CF skeleton and then deposit unevenly during the cycle plating process. Comparably, after modifying the CF with the Cu_2O layer, the lithium ions first react with Cu_2O to form Cu and Li_2O. Cu is the same component of CF and has good conductivity for electron transportation. Li_2O is lithiophobic and can induce the uniform deposition of lithium ions, resulting in a homogeneous deposition layer on the 3D current collector.

To characterize the modified coating layer on CF, X-ray diffraction (XRD) tests of the samples were conducted. Fig. 2a shows that there are typical Cu diffraction peaks (PDF 65-9743) in CF, while Cu_2O diffraction peaks (JCPDS 77-199) appear in CF-80 spectra. X-ray photoelectron spectroscopy (XPS) was used to analyze the surface components of CF-80 (Fig. 2b). The results of Cu 2p spectra show three significant peaks at 933.50, 933.12 and 932.70 eV, which can be attributed to different valence states of copper in CuO, Cu_2O and Cu, respectively. CuO is present on the surface due to the ease with which Cu_2O oxidizes in air. The TEM images indicate that the particles formed in the coating layer are irregular in shape (Fig. 2c). The corresponding HRTEM image in Fig. 2d shows lattice fringes with a spacing of 0.21 nm, which corresponds to the (200) plane of Cu_2O (JCPDS 77-199). The mappings of the coating layer particles in Fig. 2e demonstrate that both O and Cu elements are uniformly present in them. Therefore, all the above characterization outcomes confirm the existence of Cu_2O in the coating layer of CF-80.

To investigate the CF's electrochemical properties with Cu_2O coating layers formed at different temperatures, serial coating layers were prepared at 60 °C, 80 °C, 100 °C, and 120 °C (denoted as CF-60, CF-80, CF-100, and CF-120, respectively) and tested within Li–Cu asymmetric cells (Li foil as the counter electrode). The stripping processes were adjusted by setting a cut-off voltage of 0.5 V. At a current of 1 mA cm^{-2} with a Li areal plating capacity of 1 mA h cm^{-2}, the cycling results (Fig. S1–S5†) show that the CE of CF-60, CF-80, CF-100, and CF-120 is higher than that of pure CF (only retained 60% after 80 cycles). Higher CE means more stability of lithium deposition and stripping behaviors. Therefore, this indicates that lithiophilic coatings' modification is favorable for reversible lithium deposition and stripping on CF skeletons. Notably, CF-80 has the highest CE (retained 98% after 120 cycles) and the best cycling stability. Due to the use of $FeCl_3$ as an oxidant, the CF obtained becomes more brittle, making it easy for the brittle CF to penetrate the separator during battery assembly. In order to function properly, when assembling the battery, the pressure during packaging should be reduced by half. For comparison, $FeCl_3$ was used instead of FeF_3 at an optimal reaction temperature of 80 °C to obtain the product named CF-80-$FeCl_3$. As shown in Fig. S6,† the CE of the CF-80-$FeCl_3$ electrode is less than 80% and shows random oscillation after 40 cycles.

To analyse the effect of the coating layer on the electrochemical performance under different temperature conditions, optical photos and SEM images of CF, CF-60, CF-80, CF-100 and CF-120 were obtained. As shown in Fig. S7,† it is evident that the

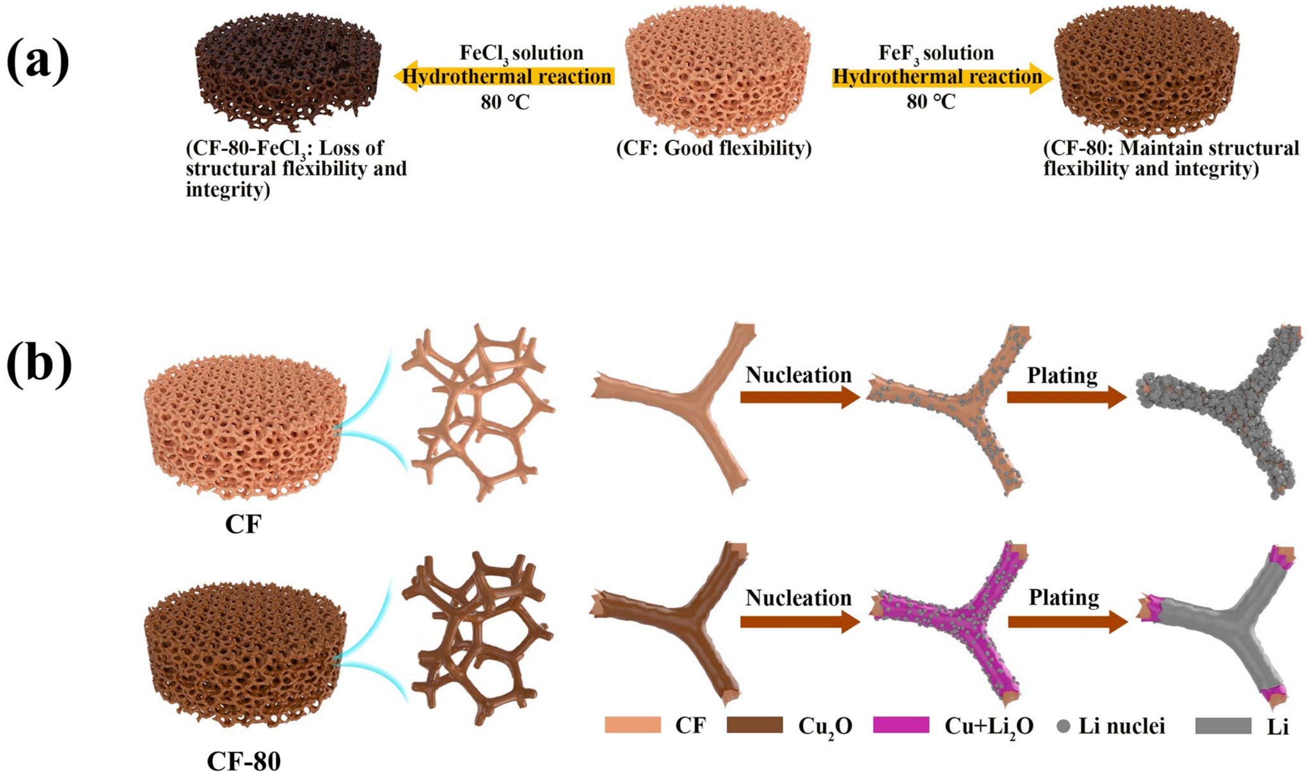

Fig. 1 (a) Two kinds of synthesis processes of the Cu_2O modified layer on CF; (b) schematic illustration of the lithium nucleation and plating process on CF and CF-80 current collectors.

surface color of samples CF-60 to CF-120 gradually darkens as the reaction temperature increases and the coating layers become more rough. At 80 °C, the product CF-80 has a relatively uniform and compact Cu_2O coating, which may contribute to its optimal coulomb efficiency. However, at 120 °C, the surface of CF-120 turns rough and black, indicating the deep oxidization

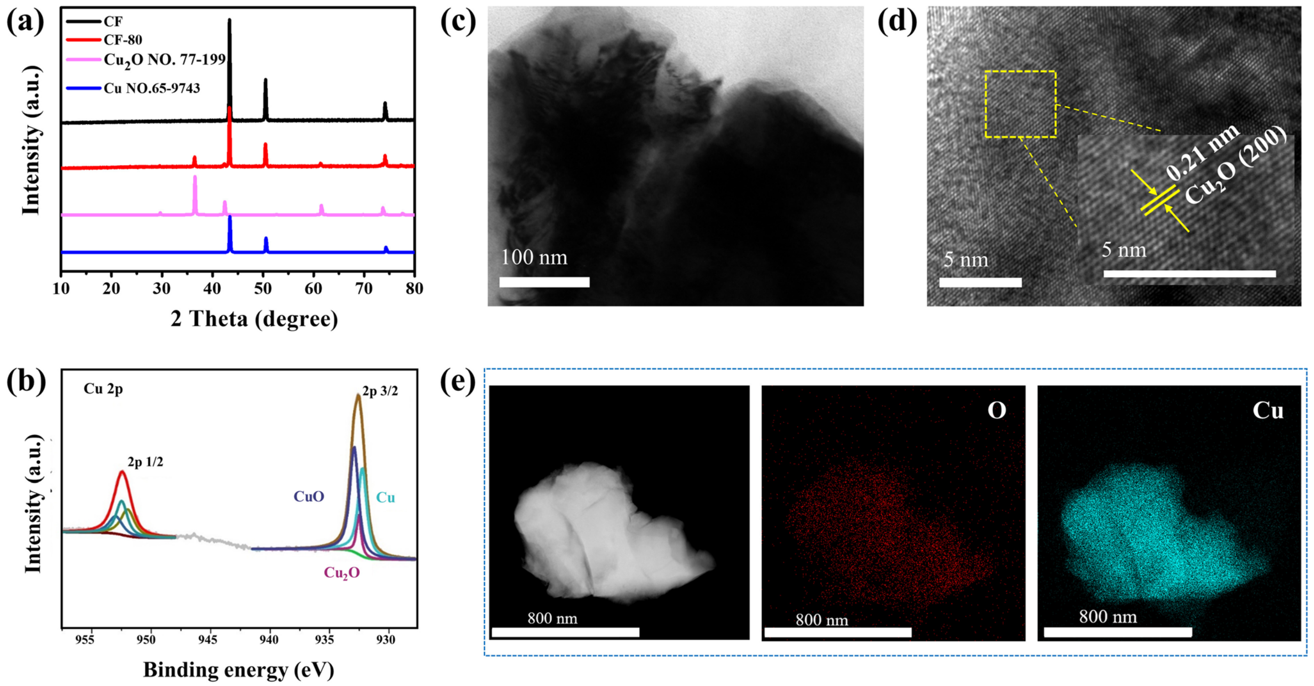

Fig. 2 (a) The XRD patterns of CF and CF-80; (b) Cu 2p XPS spectra of CF-80; (c) TEM image of particles in the coating layer of CF-80; (d) HRTEM image of particles in the coating layer of CF-80; (e) elemental mappings of particles in the coating layer of CF-80.

of brick-red Cu_2O to black CuO, which is also consistent with the XRD results depicted in Fig. S8.† With Li plates as the counter electrodes, the electrochemical impedance spectroscopy (EIS) analysis of Li–Cu asymmetric cells was conducted. Fig. S9† shows that the electrochemical impedance of the modified CF electrodes increases as the preparation temperature increases. When $FeCl_3$ replaced FeF_3 as the oxidant, CF-80-$FeCl_3$ showed a more dark color in the optical photos (Fig. S10†) than CF-80. From SEM images, it can be clearly seen that the skeleton of CF-80-$FeCl_3$ is seriously corroded and partially destroyed (Fig. S11†) and the coating layer is thicker compared with CF-80 (Fig. S12†). Furthermore, the EIS results in Fig. S9† also indicate that CF-80-$FeCl_3$ exhibits the highest impedance, which logically accounts for its exceedingly low CE. $FeCl_3$ is more soluble than FeF_3. As an oxidant for CF modification, $FeCl_3$ results in a faster reaction rate that makes it more challenging to regulate the deposition process and forms a modified layer that is comparatively less dense and thicker. When FeF_3 is used as the oxidant and the temperature is controlled, a uniform and dense coating layer can be achieved through the gradual reaction between Fe^{3+} and CF. This is crucial in enhancing the reversibility of lithium deposition and stripping. The hydrothermal reactions of Fe^{3+} and CF are shown in the following equations:

$$Cu + 2Fe^{3+} \rightarrow Cu^{2+} + 2Fe^{2+}$$

$$4Cu^{2+} + 4H_2O \rightarrow 2Cu_2O + O_2 + 8H^+$$

We proceeded to perform more detailed electrochemical characterization studies of CF-80 and pure CF, with a focus on analyzing the reasons for the improved electrochemical performance of CF-80. Firstly, the galvanostatic lithium deposition and stripping tests on CF-80 and CF electrodes were performed at 1 mA cm^{-2} with 2 mA h cm^{-2}, and the discharge–charge curves at 1st, 60th and 120th cycles are presented in Fig. 3a and b. During the 1st cycle, the nucleation overpotential for the CF electrode is 49.2 mV (Fig. 3c). In contrast, the initial lithium deposition curve of the CF-80 electrode exhibits a very smooth voltage dip at the nucleation stage, with a nucleation overpotential of only 15 mV. Furthermore, a sudden voltage drop to 69 mV was observed on the CF electrode, indicating that lithium metal begins to nucleate. The voltage then returns to a relatively stable plateau at 19.8 mV, which represents the mass-transfer-controlled overpotential. Nucleation overpotential is strongly associated with the lithiophilicity and deposition barrier of the electrode.[36] To directly compare the lithiophilicity of CF-80 and the CF, their molten Li wetting capability is shown in Fig. S13.† Molten Li uniformly spread out on the CF-80 whole surface after 40 s and the color of CF-80 changed from brick red to silver bright, while CF retains its original color after 40 s. This directly indicates that CF-80 has strong lithium affinity. Compared with the CF electrode, CF-80 has ultra-low nucleation overvoltage, which indicates that the energy barrier of lithium deposition on the CF-80 electrode is much lower, which is conducive to uniform and dense deposition of lithium metal. The chemical compositions of CF and CF-80 electrodes were analyzed through XPS techniques when they were discharged to 0.01 V (lithium metal will be deposited). The results showed that there is Li_2O on the surface of the CF-80 electrode when it is discharged to 0.01 V, while no Li_2O is detected on the CF electrode (Fig. S14†). Li_2O is designated to homogenize the electric field strength distribution within the whole electrode and facilitate Li^+ transportation.[37] Therefore, the extremely low nucleation overvoltage of CF-80 can be attributed to the following reasons: (1) CF-80 has strong lithium affinity; (2) the Li_2O formed *in situ* during the electrochemical deposition process has a low energy barrier for lithium ion migration, which is crucial for the uniform distribution of lithium ions on the electrode surface and avoids the sporadic deposition of lithium metal to a considerable extent.

The voltage hysteresis is defined as the voltage difference between the charging platform and the discharging platform. For the first 20 cycles, both CF and CF-80 show a decreasing voltage hysteresis, which may be due to the gradual activation of the electrodes (Fig. 3d). In this stage, CF-80 shows a greater voltage lag than the CF electrode, which can be attributed to the increase of CF-80 impedance by the Cu_2O coating layer. In the following cycles, the CF-80 electrode exhibits relatively smooth voltage hysteresis with cycling, whereas that of the CF electrode is relatively stable only in the next 10 cycles, and then the voltage hysteresis increases sharply. These results mean that the CF-80 electrode can inhibit the growth of an excessive SEI film compared with the CF electrode, which also suggests that CF-80 is capable of achieving uniform and dense lithium deposition, while simultaneously reducing the likelihood of side reactions. The voltage hysteresis diagram can directly reflect the difference in voltage–time curves of CF and CF-80 electrodes. The voltage–time curves of the CF-80 electrode at a current density of 1 mA cm^{-2} with a capacity of 2 mA h cm^{-2} are shown in Fig. 3e. Stable Li plating/stripping curves for more than 450 h can be achieved for the CF-80 electrode, while the voltage–time profile of the CF electrode shows significant voltage fluctuations and the overvoltage increases obviously with the cycling time (Fig. 3f). Finally, the CE of CF-80 and CF electrodes at different current densities is tested. As shown in Fig. 3g, the CE of CF-80 is higher than that of the CF electrode in the first 120 cycles. After that, the CE of CF-80 maintains at 97.6%, compared to 75% for CF at 1 mA cm^{-2} and 2 mA h cm^{-2} deposition capacity. When the current density increases by twice and the deposition capacity remains unchanged, the CF-80 electrode still has stable and high coulomb efficiency. After 100 cycles, the CE of the CF-80 electrode is maintained at 97%, while the CE of the CF electrode is only 49% (Fig. 3h).

After lithium ion deposition and stripping, the morphologies of CF-80 and CF electrodes were characterized with SEM images as shown in Fig. 4. Fig. 4a1 and a2 present the initial surfaces of CF-80 electrodes with different resolutions. When 1 mA h cm^{-2} of Li ions was plated on CF-80 at a current density of 1 mA cm^{-2}, no significant lithium deposition was observed on its surface in the SEM image (Fig. S15a†). However, after the SEM image was magnified, a small amount of smooth lithium deposition was observed, as shown in Fig. S15b.† When the Li plating capacity

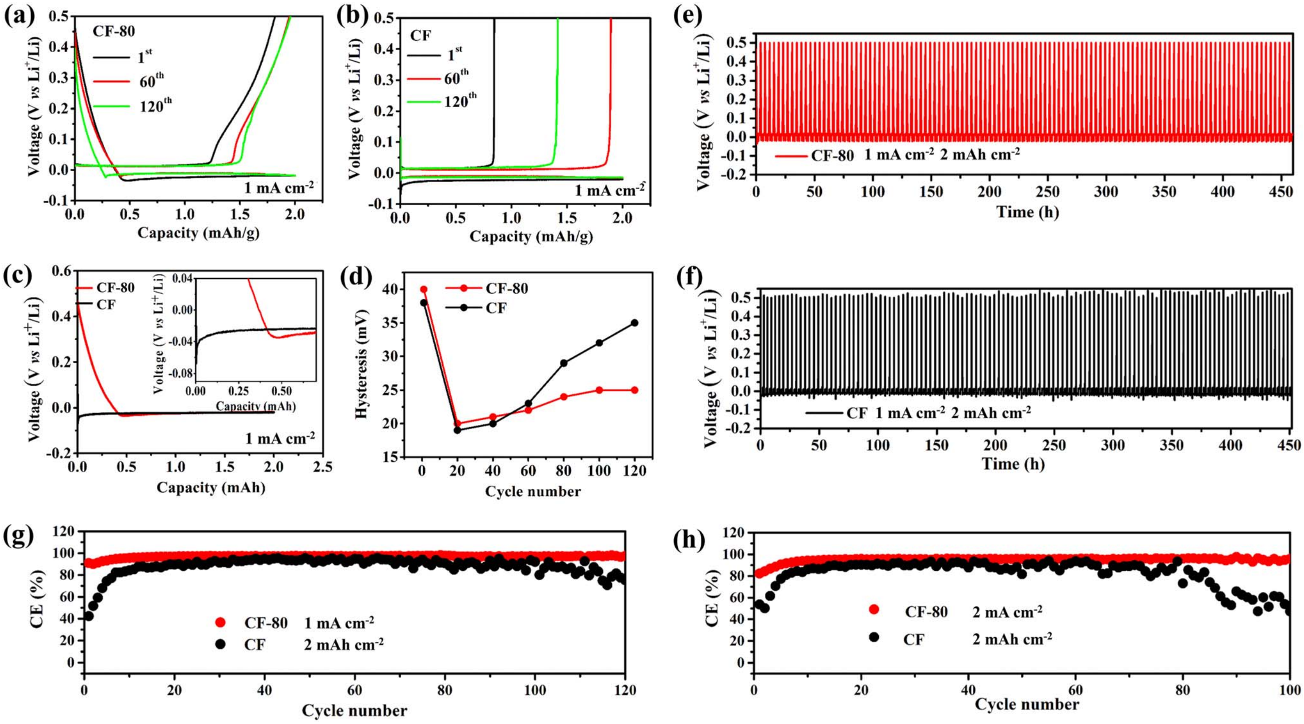

Fig. 3 Galvanostatic lithium deposition and stripping curves of (a) CF-80 electrode and (b) CF electrode at 1 mA cm^{-2} with 2 mA h cm^{-2}; (c) voltage profiles of CF-80 and CF during initial Li deposition at 1 mA cm^{-2}; (d) voltage hysteresis diagram of CF-80 and CF electrodes at 1 mA cm^{-2} with 2 mA h cm^{-2}; (e) voltage–time profile of the CF-80 electrode at 1 mA cm^{-2} with 2 mA h cm^{-2}; (f) voltage–time profile of the CF electrode at 1 mA cm^{-2} with 2 mA h cm^{-2}; (g) the CE of CF-80 and CF electrodes at 1 mA cm^{-2} with 2 mA h cm^{-2}; (h) the CE of CF-80 and CF electrodes at 2 mA cm^{-2} with 2 mA h cm^{-2}.

was increased to 2 mA h cm^{-2}, lithium deposits on the surface of CF-80 increased and thickened (Fig. 4a3). A further magnified image suggests that the lithium deposits are relatively dense and no visible lithium dendrites appear on the surface of CF-80 (Fig. 4a4). When the lithium deposition capacity is further increased to 6 mA h cm^{-2}, the compactness of the lithium deposits is further increased, and no lithium dendrites are visible on the surface of CF-80 (Fig. 4a5 and a6).

When the capacity for depositing lithium increases to 8 mA h cm^{-2}, the pores of CF-80 are filled with the deposited lithium metal, and the basic frame of CF-80 is covered with lithium metal, resulting in an even and smooth surface (Fig. 4a7 and a8). In order to test whether lithium can be deposited in an orderly manner after the CF-80 framework is completely covered by lithium metal, we further performed lithium deposition to achieve a deposition capacity of 10 mA h cm^{-2} as shown in Fig. 4a9 and a10. Obviously, the deposition of lithium is still uniform and dense. The uniform Cu_2O coating layer is believed to be the reason for the evenly distributed nucleation sites and smooth initial deposition of lithium, which is crucial for the ordered lithium plating that follows. To further demonstrate the effectiveness of the Cu_2O coating layer, we performed lithium stripping on CF-80 and observed the reversibility of the electrochemical deposition and stripping process, as shown in Fig. 4a11–a18. As the lithium was stripped away, the framework of CF-80 gradually became visible until it was completely exposed. Compared to the original CF-80 framework, there was little change in morphology. Further magnification revealed a relatively smooth surface of CF-80 with no signs of dead lithium. The reversibility of lithium deposition and stripping was excellent, corresponding to the high CE of CF-80.

For comparison, we also observed the morphologies of lithium deposition and exfoliation of CF electrodes under the same conditions. Fig. 4b1 and b2 display the initial surfaces of CF electrodes with different resolutions. The surface of the CF electrode has a large amount of lithium metal and clearly visible lithium dendrites, with a lithium deposition capacity of 1 mA h cm^{-2} (Fig. S15c and d).† As mentioned earlier, there is no visible lithium on the surface of CF-80 when 1 mA h cm^{-2} lithium is deposited. This indicates that lithium plating on the CF-80 electrode is uniform throughout the overall framework rather than selectively deposited on the top surface. As the lithium deposition capacity increases, the CF framework gradually becomes covered by the deposited lithium metal. However, the deposited lithium metal is relatively loose and generates a large number of lithium dendrites, as shown in Fig. 4b3–b10. During the electrochemical exfoliation deposition of lithium, an increase in the exfoliation amount leads to the gradual emergence of the CF framework (Fig. 4b11–b16). However, even after complete exfoliation of the CF framework, there are still non-electrochemically active dead lithium particles present on the surface (Fig. 4b17 and b18), indicating poor electrochemical reversibility of lithium ion deposition and lithium

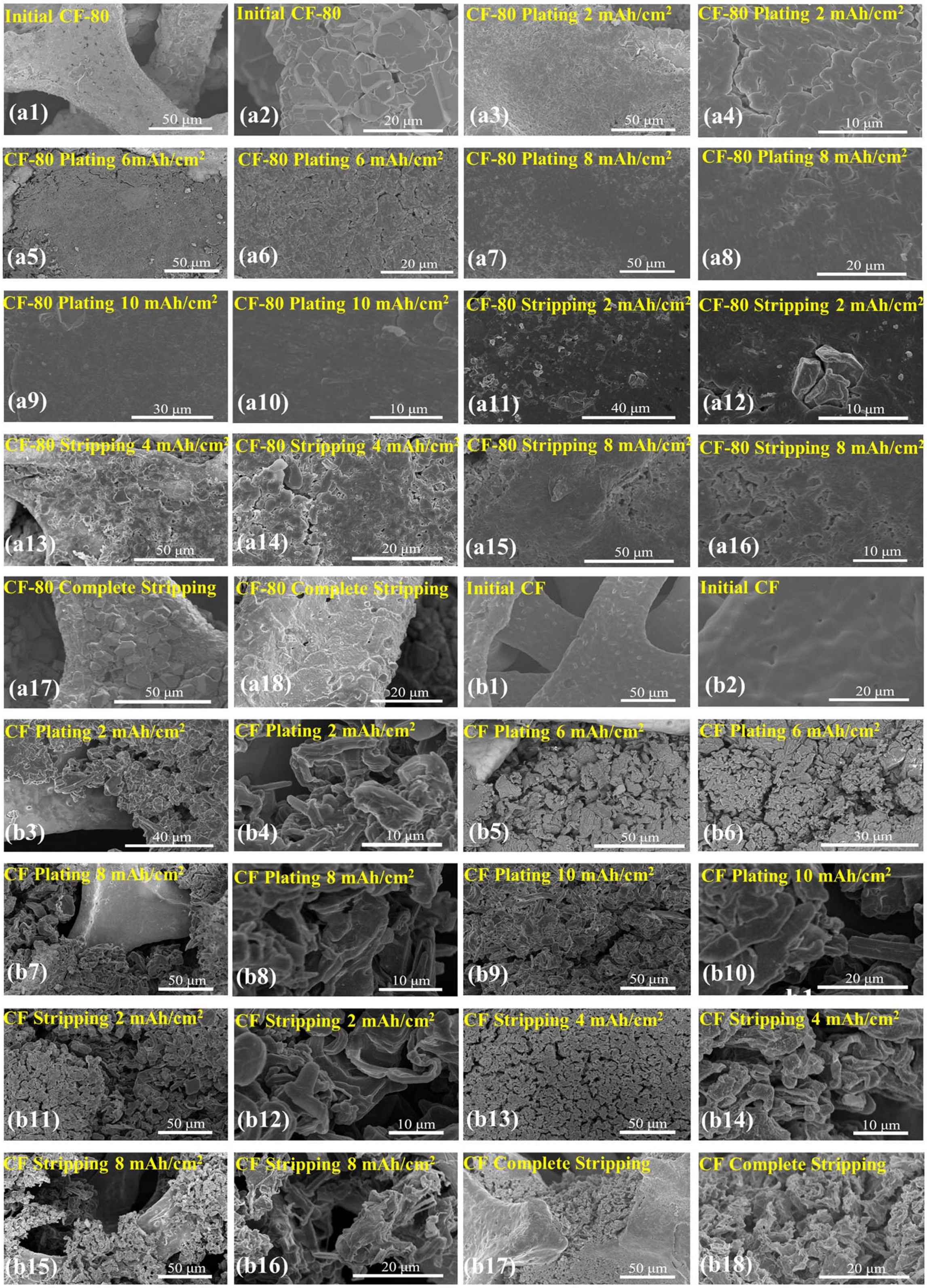

Fig. 4 (a1, a2) Top-view SEM images of initial CF-80 electrodes; (a3–a10) top-view SEM images of CF-80 electrodes after being plated at 1 mA cm^{-2}, with 2 mA h cm^{-2}, 6 mA h cm^{-2}, 8 mA h cm^{-2}, and 10 mA h cm^{-2}, respectively; (a11–a18) top-view SEM images of CF-80 after being plated with 10 mA h cm^{-2} and stripped at 1 mA cm^{-2} with 2 mA h cm^{-2}, 4 mA h cm^{-2}, 8 mA h cm^{-2}, and 10 mA h cm^{-2}, respectively;(b1 and b2) top-view SEM images of initial CF electrodes; (b3–b10) top-view SEM images of CF electrodes after being plated at 1 mA cm^{-2} with 2 mA h cm^{-2}, 6 mA h cm^{-2}, 8 mA h cm^{-2}, and 10 mA h cm^{-2}, respectively; (b11–b18) top-view SEM images of CF electrodes after being plated with 10 mA h cm^{-2} and stripped at 1 mA cm^{-2}, with 2 mA h cm^{-2}, 4 mA h cm^{-2}, 8 mA h cm^{-2}, and 10 mA h cm^{-2}, respectively.

stripping on CF. After 20 cycles at 1 mA cm^{-2} with a deposition capacity of 4 mA h cm^{-2}, the morphologies of CF and CF-80 electrodes were also investigated by SEM. As shown in Fig. S16,† a thick coating layer was observed on the surface of CF, with the amplification showing the formation of many dead lithium particles. This suggests that during the deposition of lithium on the CF electrode, more mossy lithium and dendrite lithium were produced, greatly increasing the contact area between metal lithium and electrolyte, resulting in more side reactions. The root exfoliation of the dendrite lithium will produce more dead lithium, leading to increased battery impedance and polarization. In comparison, the CF-80 electrodes exhibited a lower number of by-products on their surface, while their surface appeared smooth without any noticeable dead lithium when viewed at higher magnification. This indicates that the deposition of lithium on the CF-80 electrode was orderly and dense, resulting in a smaller contact area with the electrolyte and fewer side reactions. The cross-section views of CF and CF-80 electrodes after the deposition and stripping of lithium ions are depicted in Fig. S17.† At a current density of 1 mA cm^{-2} and a deposition capacity of 4 mA h cm^{-2}, the lithium metal on the CF-80 electrode pervades the entire cross section, whereas the lithium metal on the CF electrode is primarily accumulated on the surface. Upon removing the deposited lithium, no visible dead lithium is present on the surface of CF-80 electrodes, while a large amount of porous dead lithium persists on the surfaces of the CF electrodes. The corresponding schematic diagrams of the lithium ion deposition and stripping on CF and CF-80 electrodes in the cross section are illustrated in Fig. S18.† This is also consistent with the results of the electrodes' CE curves, as shown in Fig. S19.† The CE of CF-80 at the first cycle is as high as 94%, indicating that the deposited lithium metal is basically stripped completely, while the CE of the CF electrode at the first cycle is only 61.9%, indicating that a large part of the deposited lithium metal on the CF electrode cannot be stripped.

To better understand how lithium deposition and stripping occur on CF and CF-80 electrodes, we measured the electrode impedance of both electrodes during different cycles, as shown in Fig. 5a and b. Prior to cycling, the impedance of the CF-80 electrode was larger compared to that of the CF electrode, which may be due to the increased impedance of CF-80 with Cu_2O coating. After 20 cycles, the impedance of both electrodes decreased significantly, which could be attributed to the activation of the electrode. After 40 cycles, the impedance of the CF electrode increased while that of CF-80 remained largely the same. The increased impedance of the CF electrode might be caused by the buildup of the SEI film and the increase of dead lithium, while CF-80 remained stable, indicating that the SEI film was stable and would not generate dead lithium during the lithium stripping process. This is consistent with the results of SEM images of both electrodes after cycling.

To further assess the effectiveness of the CF-80 electrode, we introduced Li//Li and CF-80/Li//CF-80/Li symmetrical cells during cycling. The cells were cycled galvanostatically at 1 mA cm^{-2} with a capacity of 1 mA h cm^{-2}. As seen in Fig. 6a, the voltage–time curves of the bare Li and CF-80-Li symmetrical batteries were compared. The voltage hysteresis of bare Li was distinctly increased, whereas the CF-80/Li electrode had a much smaller hysteresis compared to the bare Li electrode and the voltage–time curve was more stable. In order to evaluate the practical application of the CF-80/Li anode, pure lithium anode and CF-80/Li anode were paired with NCM-811 cathodes respectively to form a full cell, and their electrochemical performance was compared. Fig. 6b displays the rate performance of the NCM//CF-80/Li battery and NCM//Li battery. At different current densities, the NCM//CF-80/Li battery has a higher discharge capacity than the NCM//Li battery. Fig. 6c presents the galvanostatic charge/discharge curves of the NCM//Li and NCM//CF-80/Li batteries at 500 mA g^{-1} in the voltage ranges of 2.7 to 4.3 V. The NCM//CF-80/Li battery's discharge capacity is higher than that of the NCM//Li battery, and it has a smaller overvoltage. As shown in Fig. 6d, the specific discharge capacity of NCM//CF-80/Li is 155.6 mA h g^{-1} in the first cycle, and it remains at 132.7 mA h g^{-1} after 150 cycles. By comparison, the NCM//Li battery's first cycle discharge capacity is 153.7 mA h g^{-1}, and it retains 122.2 mA h g^{-1} after 150 cycles. It is evident that the CF-80/Li composite electrode has excellent practical application prospects.

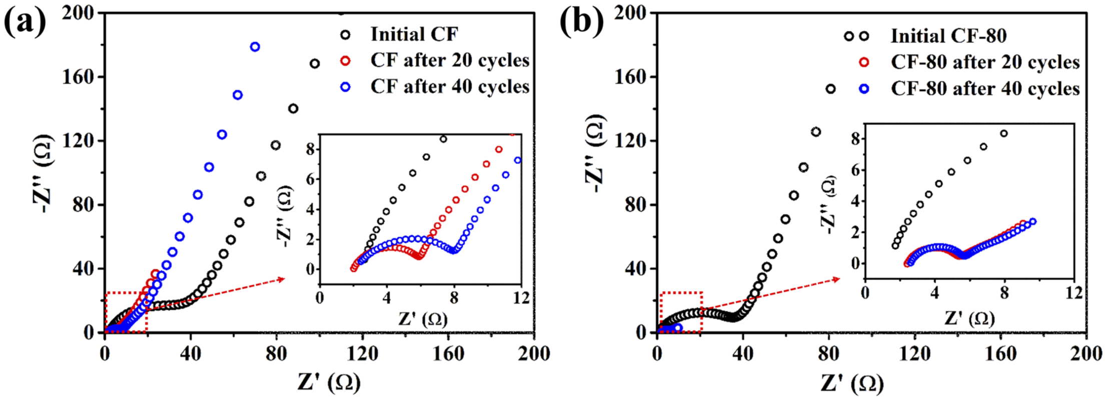

Fig. 5 EIS spectra of different cycles of (a) CF and (b) CF-80 electrodes at 1 mA cm^{-2} with 1 mA h cm^{-2}.

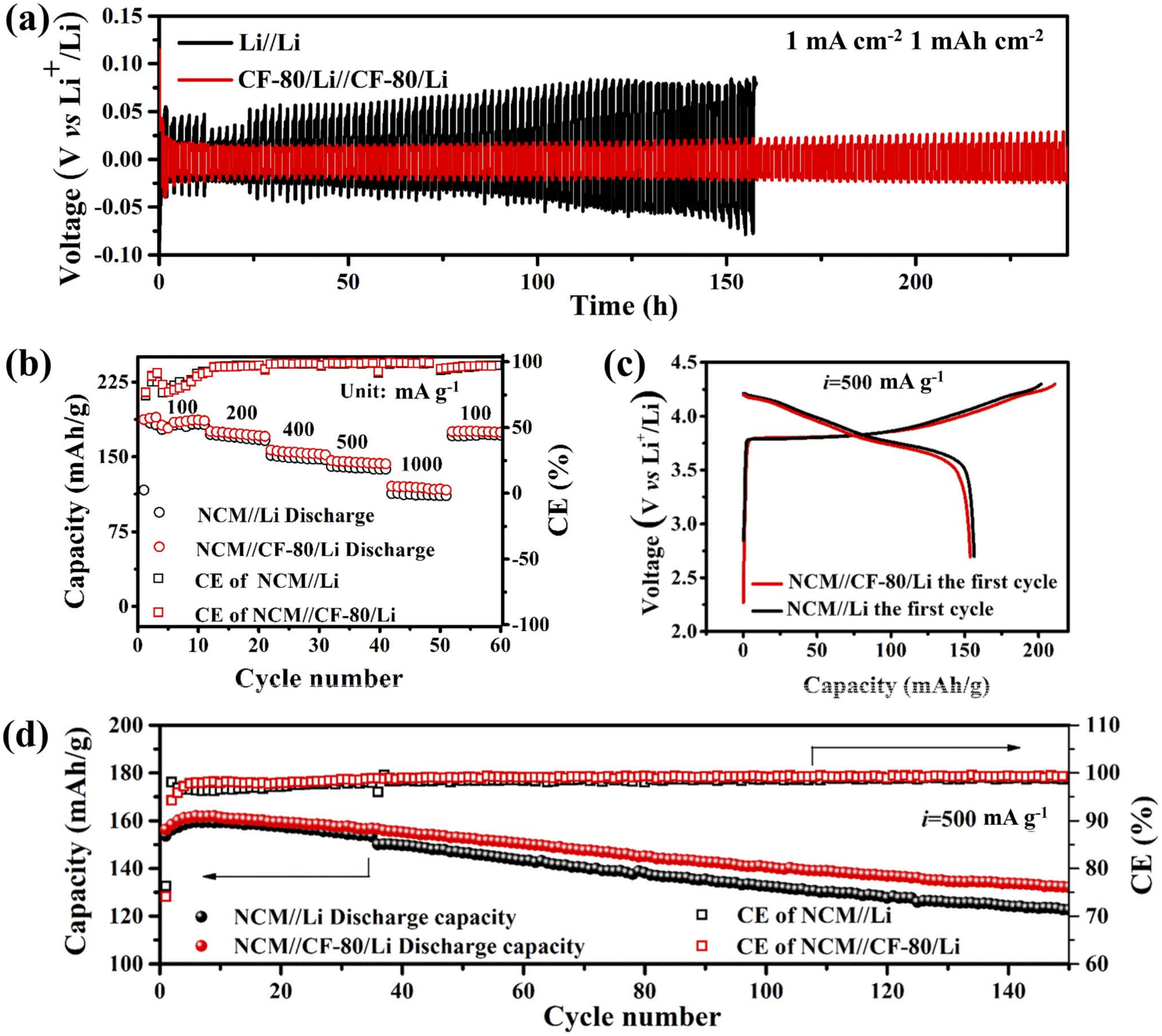

Fig. 6 (a) Voltage–time curves of the bare Li and CF-80-Li symmetrical batteries; (b) rate capability of NCM//Li and NCM//CF-80/Li full cells; (c) charge–discharge profiles at 500 mA g^{-1} of NCM//Li and NCM//CF-80/Li full cells; (d) cycling performance of NCM//Li and NCM//CF-80/Li full cells at 500 mA g^{-1}.

3. Conclusion

In summary, a 3D composite collector is successfully developed comprising lithiophilic Cu_2O coated on CF through a simple, one-step hydrothermal synthesis method. It is found that oxidants and temperature are critical factors that affect the coulombic efficiency of CF current collectors. To achieve optimal electrochemical performance of CF current collectors, it is essential to use a mild oxidant and suitable temperature to obtain a dense, uniform and appropriately thick Cu_2O coating layer. In this study, mild FeF_3 was chosen as the oxidizing agent which resulted in the formation of a dense oxide layer on the surface of CF. This can be attributed to the slower and more controlled oxidation reaction between FeF_3 and CF. Additionally, it is observed that lower reaction temperatures led to incomplete coating of the surface of copper foam, while higher reaction temperatures resulted in the formation of a thicker oxide layer, which may hinder the electrochemical reaction. The uneven coating layer fails to provide uniform nucleation sites, resulting in poor coulombic efficiency. A thick coating increases impedance and leads to severe corrosion of CF, which, in turn, destroys the structure and hinders the improvement of coulombic efficiency. Our research demonstrates that CF-80 with the optimal coating layer exhibits the highest coulombic efficiency and optimal cycle stability, with a current density of 1 mA cm^{-2} and a capacity of 1 mA h cm^{-2}. This configuration maintains a coulombic efficiency of 98% after 120 cycles in ether electrolyte without lithium nitrate. Furthermore, when the deposition capacity is doubled, the efficiency remains high at 97.6% at the same current density for 120 cycles. This straightforward and effective method for preparing Cu_2O coated CF not only serves as a guide for creating a lithium affinity coating layer, but also presents a promising approach for developing a composite 3D current collector for practical applications in the field of lithium metal batteries.

4. Experimental section

4.1. Synthesis of CF-60, 80, 100, and 120, CF-80-$FeCl_3$ and CF-80/Li

Taking synthesis of CF-80 as an example, 200 mg of FeF_3 was added to 50 mL of deionized water and stirred at 60 °C for one hour. After allowing it to stand for 5 minutes, 5 mL of supernatant was taken and added to a hydrothermal reactor. An 11 cm diameter CF slice was added, and the mixture was reacted at 80 °C for 12 hours before cooling to room temperature naturally. The prepared sample was washed multiple times with water and ethanol and finally vacuum dried at room temperature, resulting in CF-80. CF-60, CF-100, and CF-120 were synthesized under the same conditions except for the different reaction temperature, where *X* in CF-*X* represents the reaction temperature. CF-80-$FeCl_3$ was synthesized using the same method as CF-80, except that a saturated FeF_3 solution at 60 °C was replaced with a 0.1 mol L^{-1} $FeCl_3$ solution at room temperature. CF-80/Li was prepared by a facile molten infusion method for embedding molten Li into the 3D CF-80 skeleton.

4.2. Characterization

The morphologies of all samples were observed by scanning electron microscopy (SEM, HITACHI S-4800). X-ray diffraction patterns were collected using a Rigaku X-ray diffractometer (XRD, Ultima IV-185) with Cu Kα radiation. X-ray photoelectron spectroscopy (XPS, Al Kα source, 1486.6 eV) was carried out on a Thermo Escalab 250Xi instrument.

4.3. Electrochemical measurements

All coin cells (Li–Cu, Li–Li, and NCM-811-Li) were assembled with CR2032 coin cells. The CE of the asymmetrical Li–Cu half-cell was tested by depositing preset capacity of Li onto the CF, CF-*X* or CF-80-$FeCl_3$ current collector followed by stripping to 0.5 V. For the Li–Li symmetric battery, both the working electrode and counter electrode are pieces of pure lithium foil or CF-80/Li. Ether electrolyte (1.0 mol LiTFSI in a mixture of DOL and DME (1 : 1 by volume) without the $LiNO_3$ additive) was used for both symmetric Li–Li and asymmetric Li–Cu batteries, and the amount of electrolyte is 60 μL. The NCM-811 working electrodes were prepared by mixing NCM-811 (80 wt%), Ketjen black (10 wt%), and polyvinylidene fluoride (10 wt%) in *N*-methyl-2-pyrrolidone (NMP) to form an evenly dispersed slurry. The slurry was uniformly coated on Al foil and dried at 80 °C *in vacuo* overnight before being punched into the disks (diameter: 11.0 mm) and used as a working electrode. Li plates or CF-80/Li were used as the counter electrodes. The electrolyte consisted of 1 M LiPF6 dissolved in a mixture of ethylene carbonate (EC)/diethyl carbonate (DEC)/ethyl-methyl carbonate (EMC) (1 : 1 : 1 v/v/v). All batteries were assembled in a glove box filled with Ar and oxygen and water content below 0.1 ppm. Galvanostatic charge–discharge measurements were performed on a LAND CT2001A instrument at room temperature over the potential range of 2.7–4.3 V. The electrochemical impedance spectroscopy (EIS) measurement was performed in a frequency range between 10^5 and 10^{-1} Hz with a voltage amplitude of 10 mV using an electrochemical workstation (CHI6081D, Shanghai Chenhua, China).

Author contributions

Chengcai Liu: data curation, formal analysis, software, writing – original draft; Borong Wu: conceptualization, funding acquisition, project administration; Yuanxing Zhang: formal analysis, methodology; Tao Liu: formal analysis, methodology; Jingwen Cui: formal analysis, methodology; Lingjun Huang: validation; Guoqiang Tan: conceptualization, investigation; Ling Zhang: project administration, writing – review & editing; Yuefeng Su: resources, supervision; Feng Wu: resources, supervision.

Conflicts of interest

The authors declare that they have no known competing financial interests or personal relationships that could have appeared to influence the work reported in this paper.

Acknowledgements

The authors are grateful for the support from the National Natural Science Foundation of China (22179006).

References

1 B. Acebedo, M. C. Morant-Miñana, E. Gonzalo, I. R. Larramendi, A. Villaverde, J. Rikarte and L. Fallarino, *Adv. Energy Mater.*, 2023, **13**, 2203744.

2 W. Y. Wu, W. Luo and Y. H. Huang, *Chem. Soc. Rev.*, 2023, **52**, 2553; B. L. Wu, C. G. Chen, L. H. J. Raijmakers, J. Liu, D. L. Danilov, R. A. Eichel and P. H. Notten, *Energy Storage Materials*, 2023, **57**, 508.

3 F. N. Jiang, X. B. Cheng, S. J. Yang, J. Xie, H. Yuan, L. Liu, J. Q. Huang and Q. Zhang, *Adv. Mater.*, 2023, **35**, 2209114.

4 S. J. Yang, N. Yao, F. N. Jiang, J. Xie, S. Y. Sun, X. Chen, H. Yuan, X. B. Cheng, J. Q. Huang and Q. Zhang, *Angew. Chem., Int. Ed.*, 2022, **61**, e202214545.

5 Y. Zhang, L. Yu, X. D. Zhang, Y. H. Wang, C. P. Yang, X. L. Liu, W. P. Wang, Y. Zhang, X. T. Li, G. Li, S. Xin, Y. G. Guo and C. L. Bai, *Sci. Adv.*, 2023, **9**, 836.

6 A. L. Yang, C. Yang, K. Xie, S. Xin, Z. Xiong, K. Y. Li, Y. G. Guo and Y. You, *ACS Energy Lett.*, 2023, **8**, 836.

7 T. Li, X. Q. Zhang, P. Shi and Q. Zhang, *Joule*, 2019, **3**, 2647.

8 R. Xu, X. B. Cheng, C. Yan, X. Q. Zhang, Y. Xiao, C. Z. Zhao, J. Q. Huang and Q. Zhang, *Matter*, 2019, **1**, 317.

9 C. L. Wei, Y. Tao, Y. L. An, Y. Tian, Y. C. Zhang, J. K. Feng and Y. T. Qian, *Adv. Funct. Mater.*, 2020, **30**, 2004613.

10 C. Z. Wang, A. X. Wang, L. X. Ren, X. Z. Guan, D. H. Wang, A. P. Dong, C. Y. Zhang, G. J. Li and J. Y. Luo, *Adv. Funct. Mater.*, 2019, **29**, 1905940.

11 X. Zhang, Y. A. Yang and Z. Zhou, *Chem. Soc. Rev.*, 2020, **49**, 3040.

12 J. Y. Wen, Y. Huang, J. Duan, Y. M. Wu, W. Luo, L. H. Zhou, C. C. Hu, L. Q. Huang, X. Y. Zheng, W. J. Yang, Z. Y. Wen and Y. H. Huang, *ACS Nano*, 2019, **12**, 14549.

13 Z. Peng, J. H. Song, L. Y. Huai, H. P. Jia, B. W. Xiao, L. F. Zou, G. M. Zhu, A. Martinez, S. Roy, V. Murugesan, H. Lee, X. D. Ren, Q. Y. Li, B. Liu, X. L. Li, D. Y. Wang, W. Xu and J. G. Zhang, *Adv. Energy Mater.*, 2019, **9**, 1901764.

14 Y. Y. Liu, D. C. Lin, P. Y. Yuen, K. Liu, J. Xie, R. H. Dauskardt and Y. Cui, *Adv. Mater.*, 2017, **29**, 1605531.

15 Y. Huang, B. Chen, J. Duan, F. Yang, T. R. Wang, Z. F. Wang, W. J. Yang, C. C. Hu, W. Luo and Y. H. Huang, *Angew. Chem.*, 2020, **132**, 3728.

16 F. Ding, W. Xu, G. L. Graff, J. Zhang, M. L. Sushko, X. L. Chen, Y. Y. Shao, M. H. Engelhard, Z. M. Nie, J. Xiao, X. J. Liu, P. V. Sushko, J. Liu and J. G. Zhang, *J. Am. Chem. Soc.*, 2013, **135**, 4450.

17 B. Han, D. W. Xu, S. S. Chi, D. S. He, Z. Zhang, L. L. Du, M. Gu, C. Y. Wang, H. Meng, K. Xu, Z. J. Zheng and Y. H. Deng, *Adv. Mater.*, 2020, **32**, 2004793.

18 C. F. Li, S. H. Liu, C. G. Shi, G. H. Liang, Z. T. Lu, R. W. Fu and D. C. Wu, *Nat. Commun.*, 2019, **10**, 1363.

19 J. Yan, F. Q. Liu, Z. Y. Hu, J. Gao, W. D. Zhou, H. Huo, J. J. Zhou and L. Li, *Nano Lett.*, 2020, **20**, 3798.

20 C. Zhang, W. Lv, G. M. Zhou, Z. J. Huang, Y. B. Zhang, R. Y. Lyu, H. L. Wu, Q. B. Yun, F. Y. Kang and Q. H. Yang, *Adv. Energy Mater.*, 2018, **8**, 1703404.

21 H. H. Xu, Y. T. Li, A. J. Zhou, N. Wu, S. Xin, Z. Y. Li and J. B. Goodenough, *Nano Lett.*, 2018, **18**, 7414.

22 A. R. O. Raji, R. V. Salvatierra, N. D. Kim, X. J. Fan, Y. L. Li, G. A. L. Silva, J. W. Sha and J. M. Tour, *ACS Nano*, 2017, **11**, 6362.

23 Y. X. Yang, X. Huang, W. Hu, Y. C. Rao, Y. W. Wu and S. H. Ju, *Electrochim. Acta*, 2023, **441**, 141797.

24 J. R. He and A. Manthiram, *Adv. Energy Mater.*, 2019, **10**, 1903241.

25 Y. Xu, T. Li, L. P. Wang and Y. J. Kang, *Adv. Mater.*, 2019, **31**, 1901662.

26 Y. Wang, J. Tan, Z. H. Li, L. L. Ma, Z. Liu, M. X. Ye and J. F. Shen, *Energy Storage Materials*, 2022, **53**, 156.

27 D. D. Li, H. H. Hu, B. Chen and W. L. Lai, *Small*, 2022, **18**, 2200010.

28 J. Y. Chen, Y. Z. Wang, S. J. Li, H. R. Chen, X. Qiao, J. Zhao, Y. W. Ma and H. N. Alshareef, *Adv. Sci.*, 2023, **10**, 2205695.

29 J. Jung, J. Y. Kim, I. J. Kim, H. Kwon, a G. Kim, G. Doo, W. Jo, H. T. Jung and H. T. Kim, *J. Mater. Chem. A*, 2022, **10**, 20984.

30 T. T. K. Ingber, M. M. Bela, F. Püttmann, J. F. Dohmann, P. Bieker, M. Börner, M. Winter and M. C. Stan, *J. Mater. Chem. A*, 2023, **11**, 17828.

31 D. D. Wang, D. Lv, H. X. Liu, J. Yang, Y. T. Qian and Z. Chen, *Energy Storage Materials*, 2022, **49**, 454.

32 J. Shang, W. C. Yu, L. Wang, C. Xie, H. L. Xu, W. S. Wang, Q. Y. Huang and Z. J. Zheng, *Adv. Mater.*, 2023, **35**, 2211748.

33 F. Wang, J. X. Gao, Y. Liu and F. Z. Ren, *J. Mater. Chem. A*, 2022, **10**, 17395.

34 R. Zhang, X. Chen, X. Shen, X. Q. Zhang, X. R. Chen, X. B. Cheng, C. Yan, C. Z. Zhao and Q. Zhang, *Joule*, 2018, **2**, 1.

35 H. M. Zhao, Y. R. Ma, H. C. Qi, Z. Y. Xiao, H. F. Lin, J. Liu, Z. Y. Guo, L. Wang and S. H. Feng, *Chem. Commun.*, 2020, **56**, 7645.

36 C. Xu, H. Y. Wang, X. J. Liu, G. H. Liu, Z. S. Zhang, C. C. Wu and J. D. Li, *J. Power Sources*, 2023, **562**, 232778.

37 P. C. Zoua, S. W. Chiang, J. Li, Y. Wang, X. Y. Wang, D. Wu, A. Nairan, F. Y. Kang and C. Yang, *Energy Storage Materials*, 2019, **18**, 155.